JACS
JOURNAL OF THE AMERICAN CHEMICAL SOCIETY

Article

Selective C-C Coupling in Carbon Dioxide Electroreduction via Efficient Spillover of Intermediates as Supported by Operando Raman Spectroscopy

Jing Gao, Hong Zhang, Xueyi Guo, Jingshan Luo, Shaik M. Zakeeruddin, Dan Ren, and Michael Grätzel

J. Am. Chem. Soc., **Just Accepted Manuscript** • DOI: 10.1021/jacs.9b07415 • Publication Date (Web): 27 Oct 2019

is published by the American Chemical Society. 1155 Sixteenth Street N.W., Washington, DC 20036

Selective C-C Coupling in Carbon Dioxide Electroreduction via Efficient Spillover of Intermediates as Supported by Operando Raman Spectroscopy

Jing Gao[a,b], Hong Zhang[b], Xueyi Guo[a], Jingshan Luo[b,c], Shaik M. Zakeeruddin[b], Dan Ren[b,*], Michael Grätzel[b,*]

a. School of Metallurgy and Environment, Central South University, Changsha, 410083 Hunan, China
b. Laboratory of Photonics and Interfaces, École Polytechnique Fédérale de Lausanne, 1015 Lausanne, Switzerland
c. Institute of Photoelectronic Thin Film Devices and Technology, College of Electronic Information and Optical Engineering, Nankai University, Tianjin, China

*Correspondence should be addressed to D.R. and M.G.: dan.ren@epfl.ch, michael.graetzel@epfl.ch

Abstract

Developing efficient systems for the conversion of carbon dioxide to valuable chemicals using solar power is critical for mitigating climate change and ascertaining the world's future supply of clean fuels. Here, we introduce a mesoscopic cathode consisting of Cu nanowires decorated with Ag islands, by the reduction of Ag-covered Cu_2O nanowires prepared by galvanic replacement reaction. This catalyst enables CO_2 reduction to ethylene and other C_{2+} products with a faradaic efficiency of 76%. *Operando* Raman spectroscopy reveals intermediate formation of CO at Ag sites which undergo subsequent spillover and hydrogenation on the Cu nanowires. Our Cu-Ag bimetallic design enables a ~95% effective spillover of intermediates from Ag to Cu, delivering an improved activity towards the formation of ethylene and other C_{2+} products. We demonstrate a solar to chemical conversion efficiency of 4.2% for the photoelectrochemical CO_2 reduction to ethylene using water as electron and proton donor, and solar power together with perovskite photovoltaics to drive the uphill reaction.

1. INTRODUCTION

Various approaches have been proposed to alleviate the adverse effect caused by high concentration of atmospheric carbon dioxide (CO_2)[1]. One of the promising technologies is electrochemical reduction of CO_2 using renewable energy, with the production of key chemical feedstocks such as ethylene (C_2H_4) and fuels such as ethanol (C_2H_5OH) and *n*-propanol (*n*-C_3H_7OH)[2]. Exploration of efficient and robust electrocatalysts for these challenging reactions is critical for developing future renewable energy sources and implementation of CO_2 mitigation systems[3-4].

Among a wide variety of the metals, copper (Cu) has the unique capability of catalyzing the electrochemical reduction of CO_2 to hydrocarbons and oxygenates, as discovered by Hori and co-workers in the 1980s[5-6]. On a polycrystalline Cu electrode, formation of C_1 species, e.g. carbon monoxide (CO), formate ($HCOO^-$) and methane (CH_4) dominates over that of C_{2+} products including C_2H_4, C_2H_5OH and *n*-C_3H_7OH[6]. Importantly, Cu electrocatalysts derived from Cu_2O or CuO exhibit enhanced selectivity towards C_2H_4 and C_2H_5OH, while the formation of CH_4 is suppressed on these catalysts[7]. The improved C-C coupling on oxide-derived Cu was rationalized in terms of an increased surface coverage by *CO (* denotes the adsorbed species)[8-10].

The surface coverage of *CO can be further enhanced by introducing a second metal (X), such as Au, Ag and Zn that selectively catalyzes the CO_2 reduction to CO[11-17]. For example, Cu-Ag nanocoral-structured catalysts show high activity with respect to the formation of C_{2+} hydrocarbons and oxygenates[13]. However, previously reported bimetallic catalysts show unsatisfied selectivity, leading to the undesirable formation of CH_4 or CO. How to achieve optimal synergy between the Cu and X, enabling efficient C-C coupling, is yet to be investigated. Moreover, there is no spectroscopic evidence on the synergistic effect in these bimetallic systems.

Here we uniformly disperse Ag nanoparticles on the surface of a Cu_2O nanowire (NWs) scaffold *via* a galvanic replacement reaction (GRR) between Ag^+ and Cu_2O. This specific mesoscopic architecture affords an optimal corporation between Cu and

Ag, enabling large improvements of the faradaic efficiency and current density for ethylene formation. Ethylene is one of the most attractive CO_2 reduction products. It plays a key role as a feedstock for the production of polymers and high value-added chemicals and has the advantage over alcohols to spontaneously emerge as a gas from the electrolyte, thus avoiding costly separation procedures.

The improved performance of our mesoscopic catalyst is believed to be caused by the efficient CO spillover from Ag to the Cu nanowire support. *Operando* Raman spectroscopy reveals the nature of the key intermediates and their binding modes to the two catalysts, providing detailed mechanistic insight into the mode of operation of our bimetallic catalyst. Using perovskite solar cells together with sunlight as power source to drive the CO_2 reduction to ethylene on our selective CuAg cathode and water oxidation on the anode, we achieve a high solar-to-ethylene efficiency under air mass 1.5G illumination.

2. EXPERIMENTAL SECTION

2.1 General

Deionized water (18.2 MΩ cm, Purelab Ultra, ELGA) was used for washing and the preparation of solutions. All the chemicals were used without purification unless otherwise stated. The reference electrode used in this work was Ag/AgCl (saturated KCl, Pine), which was calibrated regularly against a reversible hydrogen electrode (RHE, Gasketal). All the potentials cited in this work were re-scaled against RHE unless otherwise stated.

2.2 Preparation of catalysts and solar cells

Preparation of Cu_2O FTO glass substrates (TEC-15 Ω) were etched with zinc powder (99.9%, Sigma Aldrich) and 10% HCl solution (37%, ACS reagent, Merck) to remove the conductive coating, followed by ultrasonic cleaning in deionized water for 15 min and drying under compressed air. 1.5 μm-thick Cu (99.995%) was coated by a DP650 sputter (Alliance-Concept). The sputtered Cu film was then anodized at a constant geometric current density of 8 mA cm^{-2} in 3 M KOH using a two-electrode

configuration until reaching a voltage threshold of 2.1 V (Interface 1000, Gamry). The resulting substrates were annealed at 600 °C for 4 h in Ar atmosphere (99.9999%, Carbagas) in a tube furnace (Lenton) to form Cu_2O. The temperature ramp for heating and cooling down was 10 °C min^{-1}. Cu_2O samples were then cut into slices with size of 0.4 cm × 3 cm.

Preparation of Ag-Cu_2O NWs and Au-Cu_2O NWs HNO_3 (65%, Sigma Aldrich) and $AgNO_3$ (99.995% mental basis, ABCR) were dissolved sequentially in DI water, resulting in concentrations of 20 mM and 10 mM respectively. The prepared glass slices with Cu_2O NWs were soaked into above solutions for 1 min, 3 min, 5 min and 8 min to form Ag-Cu_2O. The preparation of Au-Cu_2O is the same as the one of Ag-Cu_2O, except that aqueous 0.2 mM $HAuCl_4$ (99.99% metal basis, ABCR) solution was used instead.

Fabrication of perovskite solar cells Firstly, FTO substrates were cleaned via ultraviolet ozone treatment for 20 min. 40 nm TiO_2 compact layer was then deposited on FTO via spray pyrolysis at 450 °C from a precursor solution of titanium diisopropoxide bis(acetylacetonate) in anhydrous ethanol. A mesoporous TiO_2 layer of 150-200 nm thick was deposited on compact TiO_2 layer via spin coating of a 30 nm particle paste (Greatcell, 30 NR-D, 1:6 v/v in ethanol) at 4000 rpm for 20 s, followed by drying at 80 °C for 10 min and sintering at 450 °C for 30 min. The resulting film was treated with bis(trifluoromethane) sulfonamide lithium (LiTFSI) salt and sintered at 450 °C again for 30 min[18]. After cooling down to 150 °C, the substrates were immediately transferred in a nitrogen atmosphere glove box for the deposition of perovskite films. The perovskite films were prepared by anti-solvent method as described in our previous work[19]. Briefly, a 1.4 M triple cation perovskite $Cs_{0.05}(MA_{0.10}FA_{0.90})_{0.95}Pb(I_{0.90}Br_{0.10})_3$ precursor solution in the mixed solvent of DMF : DMSO (4 : 1, v/v) was deposited by two consecutive spin-coating steps at 1000 rpm and 6000 rpm for 10 s and 30 s, respectively. In the last 15 s of the second spin coating treatment, 200 μL of chlorobenzene was dropped onto the substrate. The films were then annealed at 100 °C for 60 min in a nitrogen-atmosphere glove box, followed by

passivation with *n*-butylammonium bromide. After the perovskite deposition, a spiro-OMeTAD solution (70 mM in chlorobenzene) doped with 20.68 µl LiTFSI (520 mg in acetonitrile) and 35.5 µl 4-*tert*-butylpyridine was spin coated at 4000 rpm for 20 s. Finally, gold top electrode with thickness of 70-80 nm was thermally evaporated under high vacuum through a shadow mask as the top anode, which defined the device area as 0.25 cm^2. The devices were encapsulated before characterization.

2.3 Material characterization

X-ray diffraction and photoelectron spectroscopy X-ray diffraction (XRD) was performed via Bragg-Brentano Geometry with a Lynexeye detector and a monochromated Cu Kα radiation source. X-ray photoelectron spectroscopy was performed on PHI VersaProbe, with an Mg Kα source. The spectra were calibrated using C 1s peak at 284.8 eV and fitted using mixed Gaussian-Lorentzian function with XPSPEAK software.

Electron microscopy The surface and cross-section of the catalysts were characterized using a scanning electron microscope (SEM, Zeiss Merlin) with an accelerating voltage of 5 kV and a probing current of 70 pA. Transmission electron microscopy (TEM) was performed on Talos (FEI), equipped with a high-angle angular dark field (HAADF) detector. The samples for TEM were prepared as follows. The films were scrapped off with a sharp blade and suspended in ethanol (Fisher Chemical). The resulting suspension was drop casted onto Au grid coated with lacey carbon (300 mesh, Ted Pella, Inc) and dried naturally.

Operando Raman spectroscopy Raman spectroscopy was carried out in a custom-built Teflon cell during CO_2 reduction in 0.1 M $KHCO_3$ using a Raman spectrometer (Reinshaw). A near infrared laser (785 nm) was used as the excitation source. A water immersion objective lens (Leica, 63×) was used for focusing and collecting the incident and scattered laser light. The electrochemical CO_2 reduction was performed at different potentials from -0.5 to -1.0 V on Cu and CuAg catalysts. Multiple spectra were collected after the reduction of oxides and one representative spectrum was shown for

each potential.

Double layer capacitance and under potential deposition The electrochemically active surface areas (ECSA) of the catalysts were estimated by double layer capacitance measurements. Cyclic voltammetry measurements were carried out at a non-faradaic potential range from -0.114 V to -0.014 V vs. RHE at scan rates of 20, 40, 60, 80, 100, 120 and 150 mV s^{-1}. The non-faradaic current densities were plotted against scan rate and the slope was determined as the capacitance value. The roughness factors were estimated by equation RF = $C_{dl}/C_{specific}$, with 30 uF cm^{-2} was used as the general $C_{specific}$[20]. Lead underpotential deposition (Pb_{UPD}) was also used to determine the number of Cu sites. Cyclic voltammetry measurements were carried out from 0 V to -0.5 V vs. Ag/AgCl at a scan rate of 10 mV s^{-1}. A Pt mesh was used as the counter electrode. The electrolyte was prepared by dissolving NaOH and $Pb(OAc)_2$ in water with the concentration of 100 mM and 1 mM, respectively, and was saturated with Ar before usage.

2.4 Electrochemical reduction of CO_2

The electrochemical CO_2 reduction was performed in a custom-built two-compartment PEEK cell. An anion-exchange membrane (Fumasep FKS-50, Fumatech) was used to separate the cathodic and anodic compartments. Electrodeposited IrO_2[21] on Ti foil was used as the counter electrode. CO_2 (99.999%, Carbagas) saturated aqueous 0.1 M $KHCO_3$ (99.99% metal basis, Sigma Aldrich) was used as the electrolyte. The volume of the catholyte and anolyte were 8 and 6 mL, respectively. CO_2 was continuously infused into both compartments at a rate of 10 mL min^{-1} (Bronkhorst High-Tech, F201CV) during the chronoamperometric measurements. The gas products of CO_2 reduction were monitored by an online gas chromatography (GC, Trace ULRTA, Thermo) periodically. A micropacked shincarbon column (Restek) was used to separate the products, which were analyzed by a pulse discharge detector (PDD, Vici). Certified gas standards with all relevant gases (H_2, CO, CH_4, C_2H_4 and C_2H_6) in CO_2 matrix (Carbagas) were used to calibrate the signals of PDD. The electrolyte, with liquid

products dissolved, was collected after electrolysis and analyzed on a ^{1}H nuclear magnetic resonance spectrometer (NMR, Avance 500, Bruker). A pre-saturation technique was used to suppress the signal of water. The area ratios of the products to DMSO or phenol internal standard were compared to the standard calibration curves to quantify the concentration of different products.

2.5 Solar-driven electrochemical reduction of CO_2

A certified silicon solar cell (Newport) was used to calibrate the light intensity of Oriel LCS-100 Class ABB solar simulator (Newport). Three perovskite solar cells were connected in series and the total effective illuminated area of unmasked solar cell was 0.75 cm^{-2}. *J-V* curves of the solar cell was scan from 0 to 3.5 V at a scan rate of 5 mV s^{-1}. Solar driven CO_2 reduction was carried out in the same H-cell described above. Electrodeposited IrO_2 anode and CuAg cathode were placed in the same compartment and the distance between two electrodes was kept at ca. 4 mm. Anion exchange membrane was excluded in this system to reduce the overall resistance. 0.2 M $KHCO_3$ was used as the electrolyte to minimize the *iR* drop and the volume of the electrolyte was 9 mL. The surface area of CuAg was adjusted to ~0.085 cm^2 to match the current supplied by the photovoltaics. CuAg was pre-reduced until reaching a steady potential before testing. *J-V* characteristic of the electrolyzer was measured via linear sweep voltammetry from 2 to 3.5 V at a scan rate of 5 mV s^{-1}.

3. RESULTS AND DISCUSSIONS

3.1 Preparation and characterization of Cu_2O and Cu_2O-Ag

Our method for preparing Cu_2O NWs and their decoration with Ag-islands, noted as Cu_2O-Ag, is illustrated schematically in Figure 1a. Cu_2O NWs were synthesized from a 1.5-μm-thick Cu film, which was firstly anodized in 3 M KOH to form $Cu(OH)_2$ NWs (Figure S1), followed by annealing at 600 ^{o}C for 4 h in Ar atmosphere[22]. The as-prepared Cu_2O showed μm-long nanowires consisting of smaller smooth particles joint by grain boundaries and Cu_2O (111) facets were identified with a lattice spacing of 0.241 nm (Figure 1b-c). Cu_2O-Ag was prepared by soaking Cu_2O into aqueous $AgNO_3$

solution for 1-8 min. Since the Cu^{2+}/Cu^{+} redox couple has a lower standard reduction potential (0.15 V vs. standard hydrogen electrode, SHE) as compared with Ag^{+}/Ag (0.80 V vs. SHE), the following galvanic replacement reaction (GRR) will take place spontaneously in acidic conditions[23]:

$$Cu_2O + 2Ag^{+} + 2H^{+} \rightarrow 2Cu^{2+} + 2Ag + H_2O$$

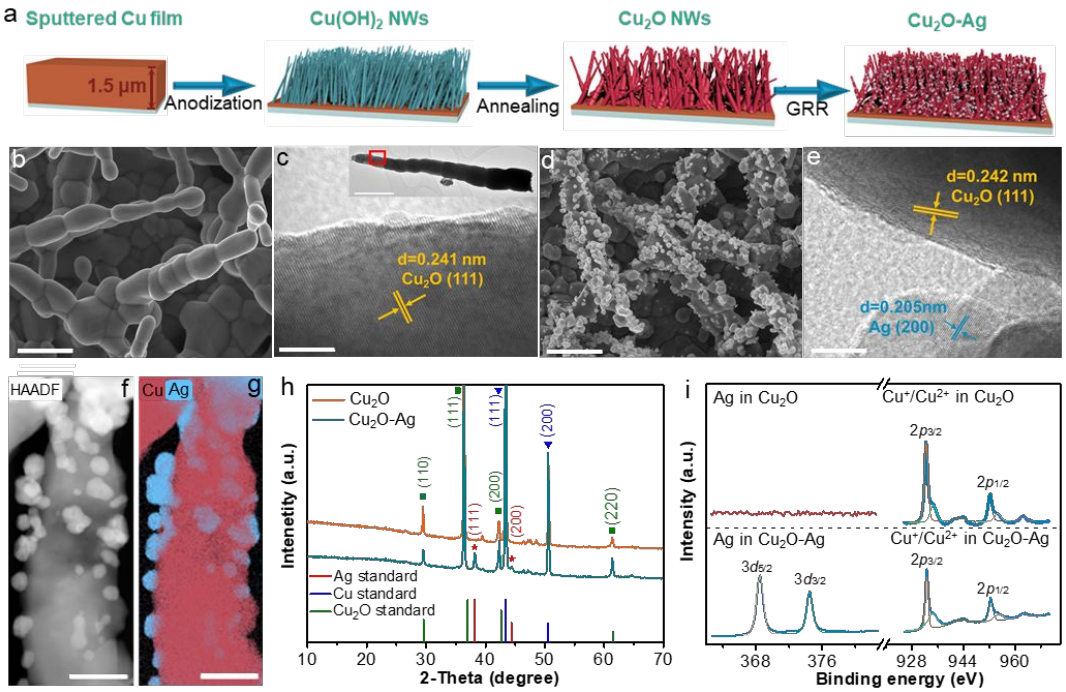

Figure 1. Structural and chemical characterization of Cu_2O and Ag-decorated Cu_2O (Cu_2O-Ag). **(a)** The schematic route for the preparation of Cu_2O and Cu_2O-Ag NWs; **(b)** SEM and **(c)** HR-TEM images of Cu_2O (insert shows low magnification TEM image); **(d)** SEM image, **(e)** HR-TEM images, **(f)** TEM-HAADF image and **(g)** respective STEM-EDX mapping of Cu_2O-Ag; **(h)** XRD patterns of Cu_2O and Cu_2O-Ag; **(i)** high-resolution Cu 2p and Ag 3d XPS spectra of Cu_2O and Cu_2O-Ag. GRR in **(a)** refers to galvanic replacement reaction. Scale bars: 1 μm for **(b)** and **(d)**, 5 nm for **(c)** and **(e)**, 500 nm for the insert in **(c)**, 200 nm for **(f)** and **(g)**. The indexes of standard XRD in **(h)** are taken from ICDD with the PDF number: 04-016-6875 for Cu_2O, 04-003-5318 for Cu and 04-016-1389 for Ag.

After 5-min GRR in 10 mM $AgNO_3$, Ag nanoparticles (NPs) with a size of 100 - 200 nm were evenly covered on the surface of Cu_2O NWs (Figure 1d). Cu_2O (111) and Ag (200) atomic layers were identified in the HRTEM image with lattice spacing of 0.242 and 0.205 nm, respectively (Figure 1e). EDS (STEM mode) mapping of Cu_2O-Ag clearly showed the dispersion of Ag NPs on the surface of Cu_2O NW (Figure 1f-g, Figure S2).

The X-ray diffractograms of Cu_2O and Cu_2O-Ag showed peaks belonging to the diffractions from Cu_2O and the Cu substrate (Figure 1h). The peaks at 38.3° and 44.4°

on Cu_2O-Ag could be assigned to Ag (111) and Ag (200), respectively. XPS peaks at ~374.5 and ~368.5 eV also confirmed the presence of Ag on Cu_2O-Ag[24] (Figure 1i). The occurrence of weak satellite features at ~942.9 and ~962.5 eV indicated the presence of small levels of CuO[25]. There is no observable shift in 2p3/2 and 2p1/2 spectra of Cu in CuAg catalyst.

Cu_2O NWs with and without Ag loading were electrochemically pre-reduced to form metallic Cu and CuAg, as demonstrated by the *operando* Raman spectra (Figure S3). Interestingly, both metallic surfaces were gradually re-oxidized upon the removal of cathodic bias, indicating the quick oxidation of the electrode surface inside the electrolyte. This is consistent with the previous reports on other oxide-derived Cu catalysts[26]. After pre-reduction, Cu was ~1.2× rougher than CuAg as measured by double layer capacitance and the total number of Cu sites were reduced on CuAg (Figure S4-S5 and Table S1).

Cu and CuAg were also characterized after CO_2 reduction reaction (Figure S6-S7). The surface of Cu grains appeared rough with the coverage of small nanoparticles, which could be attributed to the reduction of Cu_2O to Cu, as further confirmed by the disappearance of Cu_2O peaks in XRD. Moreover, CuAg is likely to be phase-separated after reduction, as proved by SEM and XRD (Figure S6). XPS measurement showed that the atomic ratio of Cu/Ag increased from 0.83 to 2.18 after 60-min electrolysis, similar observation was also reported in other bimetallic systems[15, 17].

3.2 Improved activity and selectivity for CO_2 reduction to C_{2+} products on CuAg catalyst

The activity of Cu and CuAg towards CO_2 reduction was assessed by potentiostatic measurements for 60 minutes at the selected potentials from -0.60 to -1.20 V in a custom-built electrochemical peek cell (Figure S8-S9)[22]. Aqueous CO_2-saturated 0.1 M $KHCO_3$ was used as the electrolyte. Gaseous products were quantified during electrolysis using gas chromatography (GC) and liquid products were analyzed after electrolysis using ^{1}H nuclear magnetic resonance (^{1}H-NMR, Table S2)[27].

The geometric current densities of Cu and CuAg remained stable over the duration of the 60-min electrolysis. At potentials between -1.00 and -1.20 V, the j_{total} of CuAg was 12 to 37% higher than that of Cu. Interestingly, the partial current densities for CO_2 reduction (j_{CO_2R}) on our CuAg (Figure 2a, Table S3-S4) exceeded by up to 70 % of the j_{CO_2R} on Cu at potentials < -1.00 V. The decrease of j_{CO_2R} at -1.20 V is attributed to the increased local pH at high cathodic current, which leads to the decline of the amount of dissolved CO_2 near the surface of electrode [10, 28].

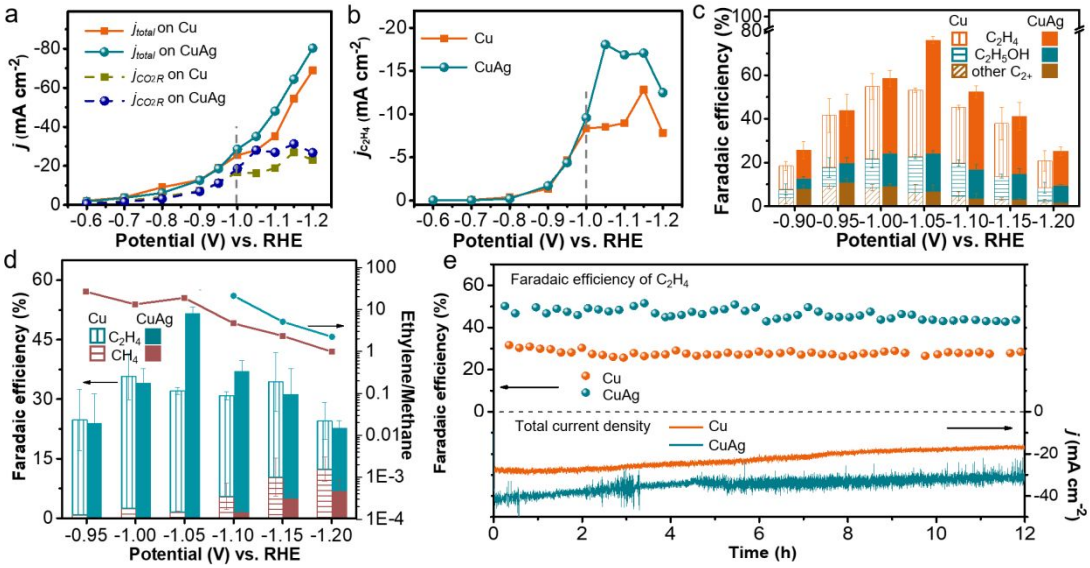

Figure 2. Electrocatalytic carbon dioxide reduction performance on Cu and CuAg catalysts. **(a)** Total current densities (j_{total}) and partial current densities of CO_2 reduction (j_{CO_2R}); **(b)** Partial current densities of ethylene ($j_{C_2H_4}$); **(c)** Faradaic efficiencies of ethylene ($FE_{C_2H_4}$), ethanol ($FE_{C_2H_5OH}$) and other C_{2+} products, **(d)** Faradaic efficiencies of methane (FE_{CH_4}) and ethylene, and the faradaic efficiency ratio of ethylene to methane ($FE_{C_2H_4}/FE_{CH_4}$); **(e)** Faradaic efficiency of ethylene and the total current densities over 12 h electrolysis as a function of applied potential on Cu and CuAg catalysts. Each data point in **(a)**-**(d)** corresponds to the average of three independent measurements and the error bars in **(c)** and **(d)** represent the standard deviations of these measurements.

A striking improvement of activity towards ethylene was observed on CuAg, as demonstrated by the enhancement of partial current density ($j_{C_2H_4}$) at potentials between -1.00 and -1.20 V (Figure 2b). The $j_{C_2H_4}$ reached a maximum value of -18.07 mA cm^{-2} at -1.05 V on our CuAg catalyst, while on Cu it was -8.53 mA cm^{-2} at the same potential, ranking our CuAg catalyst as one of the best catalysts for the conversion of CO_2 to ethylene in the reported literatures (Table S7).

The intrinsic activity reflected by the specific current density of ethylene

(normalized against the electrochemical active surface area) is also improved on CuAg at potentials < -1.00 V (Figure S10). The larger specific current density of hydrogen observed on CuAg indicates that hydrogen evolution is not suppressed at potentials <-1.00 V, which is likely due to the additional HER activity on Ag sites. This result demonstrates that our CuAg is distinct from previously reported CuAg alloy [15, 29-30]. The augmentation of ethylene formation on CuAg may be mainly attributed to the action of Ag as a co-catalyst for the production of CO, as demonstrated by our control experiment on pure Ag nanocorals (Figure S11). This local free CO near the Cu is believed to be the key intermediate for the formation of hydrocarbons[31-33]. Moreover, the mesoscopic structure of Cu also plays a critical role in the improvement of C-C coupling selectivity by elongating the residence time of CO, which presents an advantage over a planar CuAg structure (Figure S12-13)[34].

Our Ag decorated Cu nanowires also exhibit a much higher faradaic efficiency for the formation of ethylene ($FE_{C_2H_4}$) compared to the Ag-free reference (Figure 2c). With the bare Cu nanowire cathode, a maximum $FE_{C_2H_4}$ of 33% was achieved on Cu at -1.00 V and the total FE of C_{2+} products approached 58%, which is consistent with previous reports using different types of oxide-derived Cu catalysts[7, 26, 35-36]. The maximum $FE_{C_2H_4}$ was greatly improved to 52% on CuAg at -1.05 V, with an impressive total FE of ~76% for all C_{2+} products. Interestingly, the faradaic efficiencies of ethanol on CuAg and Cu catalysts do not show much difference[37]. This is likely due to the lack of Cu-Ag phase boundaries, which are believed to be critical in improving the ethanol formation[12].

It is noted that the onset potential of methane production shifted from -0.95 V on Cu to -1.10 V on CuAg and the faradaic efficiency of methane (FE_{CH_4}) on CuAg was much lower compared with that on Cu (Figure 2d). For example, FE_{CH_4} decreased from 5.47% on Cu to 1.67% on CuAg at -1.10 V. The combined effects of boosting C_2H_4 while suppressing CH_4 formation resulted in a large enhancement of the selectivity for ethylene expressed by $FE_{C_2H_4}/FE_{CH_4}$ on our CuAg catalyst.

Both Cu and CuAg showed good stability with continuous production of ethylene over 12 h electrolysis (Figure 2e). The $FE_{C_2H_4}$ on CuAg decreased from ~50% to ~44% after 12 h. The robustness of CuAg was confirmed by SEM after stability test (Figure S7), which showed similar morphology with the CuAg catalyst after 1 h electrolysis.

3.3 *Operando* Raman spectroscopy of Cu and CuAg catalysts in CO_2 reduction

O*perando* Raman spectroscopy was carried out at different potentials after the reduction of oxides to reveal the reaction intermediates during CO_2 reduction, thus gaining mechanistic insight on the catalytic differences between Cu and CuAg. A custom-built Raman setup was used to probe the surface of Cu and CuAg during CO_2 reduction at different potentials in 0.1 M $KHCO_3$.

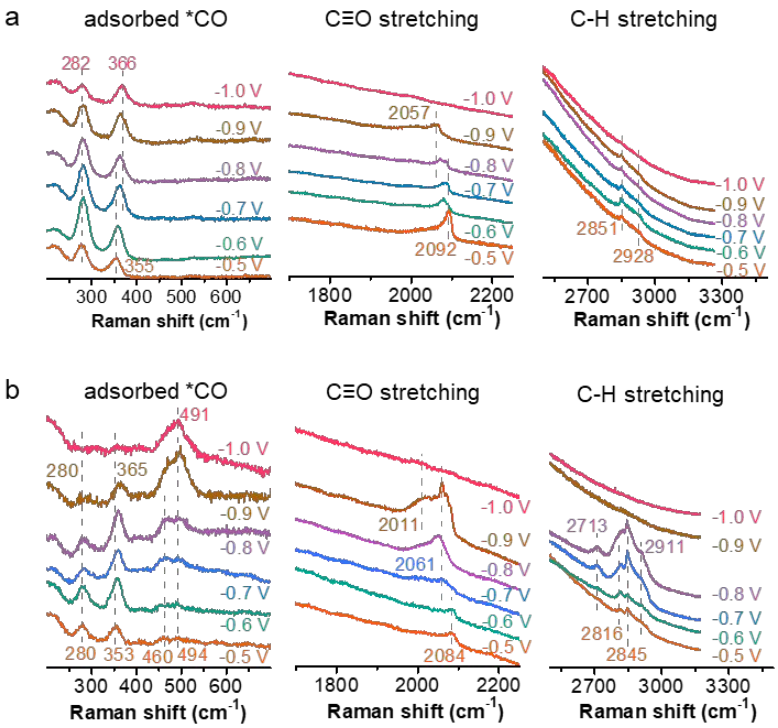

Figure 3. *Operando* Raman spectroscopy of Cu and CuAg catalysts. *Operando* Raman spectra of **(a)** Cu and **(b)** CuAg during electrochemical reduction of CO_2 at different potentials in 0.1 M $KHCO_3$. The spectrum was collected at three different regions: low-frequency 200-700 cm^{-1}, medium-frequency 1700-2300 cm^{-1} and 2500-3500 cm^{-1}. CO_2 was continuously flowed to the electrolyte. A near infrared laser (785 nm) was used as the excitation source. All the spectra were collected after sufficient time of electrolysis to ensure the reduction of oxides. Each spectrum is the representative of multiple measurements at different time scale of electrolysis.

The presence of adsorbed CO on Cu was demonstrated by the appearance of Raman peaks located at 282, 355-366, and 2057-2092 cm^{-1}, which correspond to the restricted rotation of adsorbed *CO on Cu, Cu-CO stretching and C≡O stretching,

respectively (Figure 3a)[38]. These peaks were also observable on CuAg catalyst, showing the vibration of adsorbed CO on Cu sites (Figure 3b). Besides, more peaks at frequencies of 460, 491-494 and 2011 cm^{-1} appeared. The new peaks are likely to originate from adsorbed CO on Ag surface, as supported by our control experiment on rough Ag surface (Figure S14)[38-39]. Our observation is significantly different from previous-reported CuZn bimetallic catalyst which showed no detectable adsorbed CO on Zn site[11]. The reason could be the slightly stronger binding of CO onto Ag as compared with Zn[40]. It is also noted that the multiple binding sites of CO (peaks at 2011, 2061 and 2084 cm^{-1}) are not solely from Cu but also from Ag sites, which is different in nature as compared with recently reported CuAg catalyst[41].

The vibration of C-H was also observed at region from 2700 to 3000 cm^{-1} (Figure 3a-b). Two peaks at ~2850 and ~2920 cm^{-1} were detected on both Cu and CuAg catalysts. The peaks were more obvious on CuAg than that on Cu, indicating a larger surface population of reaction intermediates containing C-H bond (such as *CHO, $*C_2H_2O$, etc) on CuAg catalyst. Remarkably, two new peaks at 2713 and 2816 cm^{-1} appeared on CuAg, which also indicates the enhanced coverage of CH-containing intermediates. It is believed that these intermediates are critical for the formation of hydrocarbons[42]. However, a more precise assignment of these peaks is extremely challenging due to the complexity of reaction intermediates that contains C-H bond.

All the signals in our Raman spectra largely benefit from the surface-enhanced Raman scattering (SERS) effect of our nanoparticulate Cu substrate. It is noted that Ag nanoparticles could also introduce extra SERS on CuAg[43]. However, the differences of signal to noise ratio of Cu-C vibrational signals on CuAg and Cu cast doubt on this proposition (Figure 3a-b). It is unlikely that the appearance of new peaks on Cu-Ag is due to the SERS caused by Ag nanoparticles, which is further corroborated by the observation of only traces of peaks at 2713 and 2816 cm^{-1} on a thin Cu_2O that is deposited onto an electrochemically-roughened Ag substrate (Figure S15-16).

It is also noted that the potentials where these new peaks appeared (-0.5 to -0.9

V) on CuAg are more positive than the potential where the formation of ethylene greatly enhanced (-1.05 V, Figure 2). This is not surprising since these intermediates undergo very fast kinetics of being reduced at potentials <-1.0 V. Similar phenomenon has also been reported for intermediates involved in hydrogen evolution, oxygen evolution and CO_2 reduction[44-47].

Thus, our Raman spectra demonstrated that the formation of key intermediates ($C_xH_yO_z$) towards hydrocarbons and oxygenates are significantly improved on the surface of CuAg catalysts, due to that the desorbed CO from Ag spillover to Cu sites and the adsorbed CO intermediates on Cu undergo further reduction. However, little kinetic information on the process of CO spillover can be inferred from the Raman spectrum.

3.4 Proposed mechanism of CO_2 reduction to C_2H_4 on CuAg catalyst

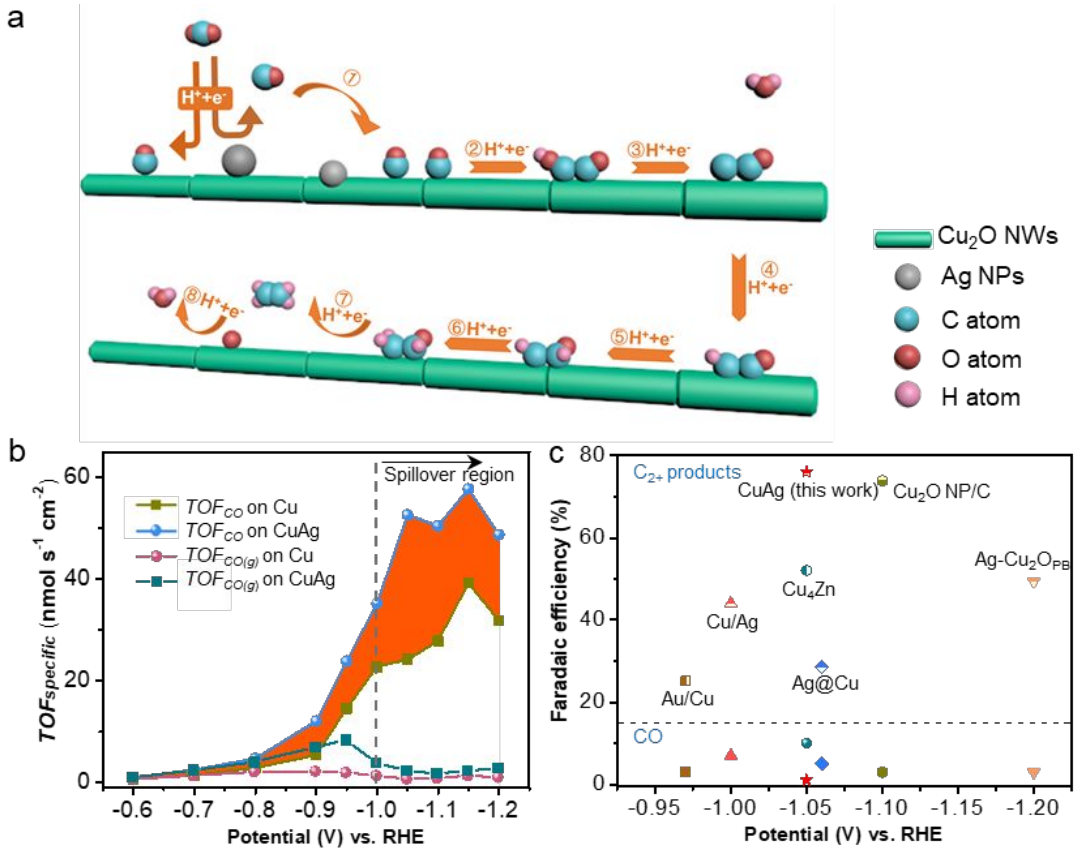

Figure 4 (a) Proposed mechanism for the electroreduction of CO_2 to ethylene on CuAg catalyst: Step 1, the mobile gas CO produced from Ag sites readsorbs on Cu sites; step 2, CO dimerize through C-C bond formation with electron transfer, forming adsorbed *CO-COH after proton transfer; step 3, protonation of *CO-COH, accompanied by a H_2O desorption; step 4-7, continuous protonation of the intermediates, resulting in C_2H_4 formation and leaving an adsorbed *O; step 8, protonation of *O adsorbate, forming *OH and then H_2O. The number of proton and electron in each step is not balanced. **(b)** Quantitative

analysis of *in situ* CO generated from Ag sites in CuAg: production rates of CO (including *CO intermediates and gaseous CO) and gaseous CO as a function of the potential on Cu and CuAg catalysts, the shaded region highlights the improvement of 'CO production' after Ag was incorporated into oxide-derived Cu. **(c)** Comparison with state-of-the-art copper and bimetallic copper-X catalysts: Faradaic efficiency of C_{2+} products and CO[11-14, 17].

Based on the electrocatalytic performance and *operando* Raman spectroscopy results, we propose a sequential catalytic mechanism for the reduction of CO_2 to C_2H_4 for our CuAg bimetallic system (Figure 4a). Incoming CO_2 is firstly reduced to CO on either Cu_2O derived Cu or Ag sites by transfer of 2 electrons and 2 protons [48-49]. CO produced on Ag is likely to desorb due to the weak binding between CO and Ag[40], resulting in an increased local CO concentration near the surface of electrode. The local CO may re-adsorb on Cu sites (step 1), resulting in a high surface coverage of *CO[50]. At a sufficiently high overpotential, i.e. < -1.0 V, CO dimerizes with the formation of C-C bonds (step 2). This is supported by the observation of protonated CO dimer during CO_2 reduction by *in situ* FTIR spectroscopy, reported by Koper and co-workers[46]. The appearance of large amounts of CH-containing intermediates in the Raman spectra indicates the further reduction of CO or CO dimers, leading to the formation of ethylene (step 3-8) [48].

3.5 Efficient CO spillover on CuAg catalyst

Based on the preceding results, we believe that an ideal Cu-X bimetallic system should enable the reduction of the entire CO that is generated from X. In other words, the best synergy should exhibit 100% efficiency of CO spillover from X to Cu. To uncover the fundamental insights into the synergy between X and Cu, we quantitatively analyze the efficiency of CO spillover from Ag to Cu. The total production rate of CO (TOF_{CO}), including *CO intermediate (TOF_{*CO}) and gaseous CO ($TOF_{CO(g)}$), on Cu and CuAg catalysts was calculated against electrochemical active surface areas. For reasons of mass balance:

$$TOF_{*CO} = TOF_{CO} - TOF_{CO(g)}.$$

The *TOF* difference between Cu and CuAg is defined as ΔTOF_{CO}. As shown in Figure 4b, TOF_{CO} on CuAg was much higher than TOF_{CO} on Cu alone when the applied

potential was more negative than -1.0 V, showing a striking enhancement from 24.2 nmol s^{-1} cm^{-2} on Cu to 52.6 nmol s^{-1} cm^{-2} on CuAg at -1.05 V (ΔTOF_{CO} = 28.4 nmol s^{-1} cm^{-2}, shown in Table S8). On the other hand, the production rate of gaseous CO only increased from 0.7 nmol s^{-1} cm^{-2} on Cu to 2.3 nmol s^{-1} cm^{-2} on CuAg. Therefore, out of the enhancement of TOF_{CO} (28.4 nmol s^{-1} cm^{-2}), only 1.6 nmol s^{-1} cm^{-2} is released as CO gas, demonstrating that ~95% of the CO produced on Ag sites is further reduced by Cu. We attribute this efficient CO spillover to be the major reason for the enhanced activity towards the formation of ethylene on CuAg.

It is noted that spillover of CO occurs only at a narrow potential range from -1.0 V to -1.2 V (Figure 2a-b, Table S8). At potentials > -1.0 V, the specific current densities for C_2H_4 formation are almost identical on two catalysts. This demonstrates the small effect of Ag on the production of C_2H_4, which is instead mainly limited by the reaction rate of further CO reduction on Cu though Ag catalyzes CO_2 reduction to CO in the vicinity of the Cu sites at potentials > -1.0 V.

As for the detailed pathway for CO spillover from Ag to Cu, here we propose two synergistic routes: 1) CO produced on Ag nanoparticles first desorbs into the electrolyte, followed by diffusing and re-adsorbing on the vicinal Cu sites; 2) *CO that adsorbed on Ag directly diffuses through the boundaries of Cu and Ag, and transfers to Cu sites. The latter spillover pathway is more commonly studied for *H spillover in electrochemical hydrogen evolution[51-52]. Here, in our system, the number of Ag sites adjacent to Cu is much less compared to the sum of active Ag sites. Considering that CuAg delivers a remarkable CO spillover efficiency, the majority of CO is likely to spillover *via* the former pathway.

Similar CO spillover efficiency could also be achieved on CuAu bimetallic catalysts that were prepared in similar ways under the identical test conditions[53]. After optimizing the galvanic replacement reaction between Cu_2O and $HAuCl_4$, small Au nanoparticles with size around 30~50 nm were uniformly decorated on the surface of Cu_2O NWs (Figure S17). Formation of ethylene and ethanol was maximized on CuAu

electrode at -1.05 V with faradaic efficiencies of 38.70% and 22.60%, respectively (Figure S18). The efficiency of CO spillover based on specific TOF was calculated to be >90% at -1.05 V (Figure S19).

3.6 Comparison with the state-of-the-art catalysts

Our CuAg is also compared with other Cu-based catalysts reported in literatures in terms of faradaic efficiency[11-14, 17]. Figure 4c depicts the faradaic efficiencies of C_{2+} products and CO at the optimal potential for C_{2+} formation on other Cu and CuX (X = Au, Ag and Zn) catalysts. Our catalyst ranks as one of the best catalysts for ethylene production in terms of faradaic efficiency and current density. Moreover, the intrinsic activity as reflected as the specific current density for ethylene formation on CuAg also increased by > 2 times compared to oxide-derived Cu electrodes (Figure S10).

The faradaic efficiency of CO is extremely low (~1.0%) on our CuAg catalyst as compared with the oxide-derived Cu-Zn, which showed 10.4% of CO even at the optimal potential for ethanol production[11]. It is also noted that catalysts such as Ag@Cu and Au/Cu exhibited only ~28.6% and ~18.3% of C_2 products, though the faradaic efficiency of CO is relatively low (3.2% and 7.0%), respectively[14, 17]. We postulate that the reason could be that the active sites of metallic Cu is not as efficient as that of oxide-derived Cu, in terms of favoring C-C coupling to form C_2 products[13, 15]. Moreover, loss of faradaic current due to the competing hydrogen evolution reaction remains a major challenge for CO_2 reduction to multi-carbon products. For example, around 35% ~ 44% H_2 were recorded on the reported Cu-Ag and Cu-Au catalysts, indicating the poor suppression of H_2 in these bimetallic system[12-14, 17].

Another insight can be gained by comparing our CuAg and CuAu catalysts. We observed that the selectivity towards C_{2+} products on CuAu was higher at more positive potentials than that on CuAg catalyst (Figure S20). A possible reason is that the favored potential for producing CO on Au is more positive than that of CuAg (Figure S21). The lower overpotential for CO production at Au sites is beneficial for the accumulation of *CO adsorbates at less negative potential range. Since Au nanoparticles favor hydrogen

evolution instead of CO production when the potential is negative than -1.0 V, the faradaic efficiency of ethylene is less on CuAu compared with CuAg[53]. The comparison between CuAu and CuAg highlights the importance of how well the optimal potential of CO production and best potential for C-C coupling on Cu sites are matched.

Based on the above discussions, we highlight critical factors for designing efficient and selective bimetallic catalysts for the formation of C_{2+} products. The first factor is the choice of Cu and X. The use of oxide-derived Cu is more favored over metallic Cu and X should not be too effective in terms of catalyzing the formation of CO. The structure of the two counterparts, i.e. particle size, surface roughness and defects, is also critical. Here, Cu_2O nanowires that consisted of small grains are chosen since this meso-structure facilitates the mobility and adsorption of CO intermediates[8]. The last important factor is that optimal potential for CO production on metallic co-catalyst should lie closely to the optimal potential window for C_{2+} products formation on copper sites.

3.7 Photosynthesis of C_2H_4 from CO_2 using water as electron and proton source

The ultimate research goal for discovering selective electrocatalysts for CO_2 reduction is to accomplish CO_2 fixation using renewable electricity. Recently, some encouraging reports achieved high energy efficiencies for solar-driven CO_2 reduction to carbon monoxide and formate, whose formation requires relatively low overpotentials (Table S9)[22, 54-57]. Compared with carbon monoxide and formate, ethylene is much more attractive due to its high commercial value and widespread industrial use[58]. However, achieving solar-driven CO_2 reduction to ethylene using water as electron and proton source with appreciable conversion efficiency remains a challenge[13, 21, 59]. The solar to ethylene (STE) conversion is mainly limited by high overvoltage losses at the cathode material and the solar to electric power conversion efficiency (PCE) of the photovoltaic. Additional losses may arise from a mismatch between the operating voltage and the voltage at the maximum power point (V_{mpp}) of the solar cell, even though these can be largely avoided by electronic management of

the photovoltaic power output. Here we achieved a benchmark solar to ethylene conversion efficiency by employing our efficient CuAg catalysts and addressing the discrepancies in the previous reports. Electrodeposited IrO_2 was used as the anode to catalyze water oxidation. The overall reaction and the corresponding equilibrium cell potential corresponding to the standard free energy of the CO_2 conversion reaction are[60]:

$$2CO_2 + 2H_2O = C_2H_4 + 3O_2 \ (E = 1.15 \text{ V}, \Delta G^* = +1323 \text{ kJ mol}^{-1})$$

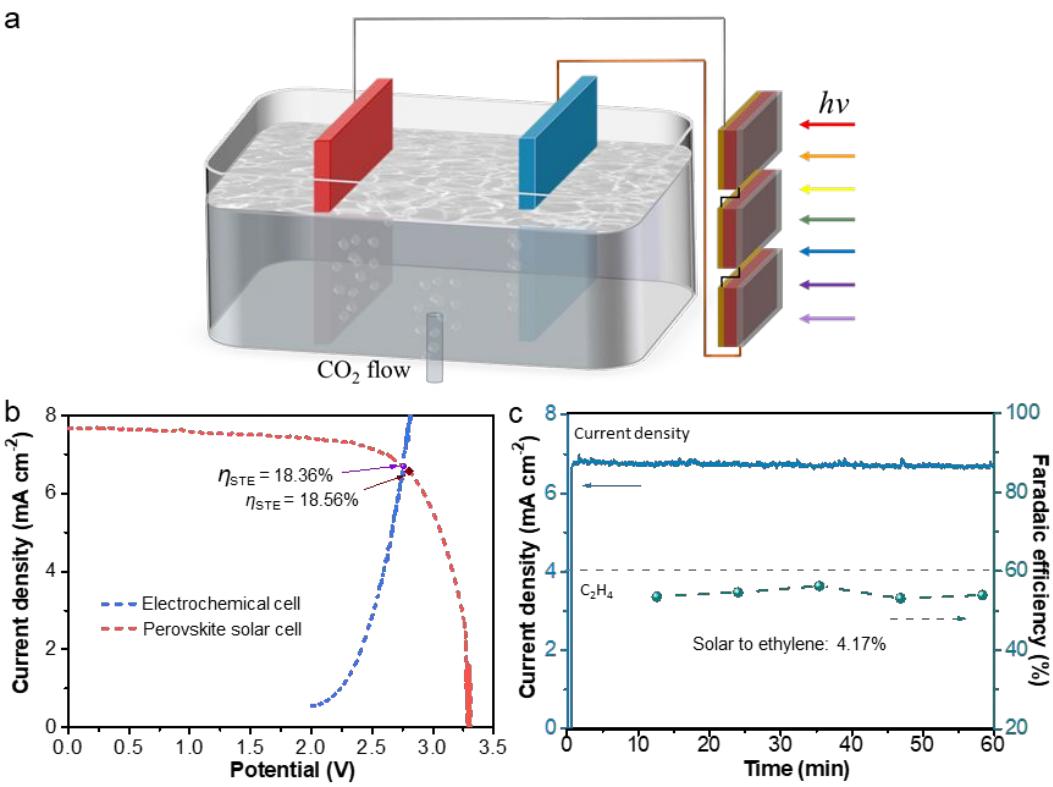

Figure 5. Characterization of solar driven CO_2 reduction system. **(a)** *J-V* curve of three connected perovskite solar cells under AM 1.5G 1 Sun solar illumination, overlaid with *J-V* curve of CuAg cathode and IrO_2 anode in the two-electrode configuration, the surface area of CuAg was normalized to the total illuminated area of three solar cells (0.75 cm^2). The maximum power point of the photovoltaics and the operating point of the complete system are designated with dots. **(b)** Operating current density and faradaic efficiency of ethylene of the complete system during the initial 1 h test.

0.2 M $KHCO_3$ was used as the electrolyte to improve the conductivity and the catalytic activity of CuAg catalyst is slightly different from that observed in 0.1 M $KHCO_3$ (Table S10), which is consistent with many previous works[3]. To further minimize the *iR* drop between two electrodes, ion exchange membrane was excluded. An overall cell voltage of about 2.8 V is required with the operating current density varying from -40 to -60 mA cm^{-2} in order to maintain a ~50% faradaic efficiency for

ethylene generation (Table S10). This cell voltage value (V) can be divided into four parts:

$$V = E + \eta_{ethylene} + \eta_{oxygen} + iR$$

Where E represents the standard thermodynamic cell potential for the conversion of CO_2 and H_2O to O_2 and C_2H_4, $\eta_{ethylene}$ and η_{oxygen} represent the overpotentials for ethylene formation and oxygen evolution, and iR represents the ohmic loss between two electrodes.

Based on the voltage requirement of ~2.8 V, we carefully designed perovskite solar cells with V_{mpp} of ~950 mV to ensure that three of them connected in series provide the suitable voltage for the combined photolytic CO_2 reduction system (Figure 5a)[19]. The connected solar cells show an open-circuit voltage of 3.30 V and a short-circuit current of 7.66 mA cm^{-2} under AM 1.5 G illumination (Figure 5b), yielding a solar-to-electricity conversion efficiency of 18.56% from the forward curve. It should be noted that the surface area of the cathode is also adjusted to match the current generated by the solar cells.

The predicted operating point of the solar driven CO_2 reduction is defined by the intersection of the J-V curve of the electrolyzer and the perovskite solar cells (Figure 5b). The operating point (6.67 mA cm^{-2} at 2.76 V) matches well the maximum power output metrics of the perovskite solar cells (6.63 mA cm^{-2} at 2.80 V), indicating the optimum solar-to-electricity conversion process in our integrated device. The performance was further characterized without applying any external bias under AM 1.5G light illumination (Figure 5c). An average faradaic efficiency of 54% for ethylene was achieved at a stable current density of 6.68 mA cm^{-2} during 60 min test, demonstrating that the electricity-to-fuel is also under the optimal condition. This combined system delivers a benchmark solar-to-ethylene conversion efficiency of 4.17%. Totally, a solar-to-fuel conversion efficiency of 7.78% was achieved accounting for all reduction products (Table S11). This performance ranks our unassisted photolytic system the most efficient solar-to-ethylene system so far reported (Table S9),

with the added advantage that our light harvesting materials are earth-abundant in contrast to photo-electrolysis employing tandem III-V semiconductors as absorber material.

4. CONCLUSIONS

In this work, we developed a Cu_2O derived CuAg bimetallic catalyst produced by galvanically replacing Cu(I) ions in the Cu_2O nanowires by Ag(I) from a $AgNO_3$ solution. Synergistic interaction between oxide-derived Cu nanowires and metallic Ag islands deposited on their surface led to a striking enhancement in the selectivity and activity for CO_2 reduction to ethylene, giving a faradaic efficiency of ~52% and a current density of -18.07 mA cm^{-2} at -1.05 V. Overall, a faradaic efficiency of ~76% for C_{2+} products was obtained with on CuAg. We assign the enhancement of performance of our CuAg catalyst to the efficient CO spillover from Ag to Cu, with ~95% of the CO formed on Ag being transferred and reduced on Cu. Moreover, the mesoscopic structure of our catalyst also engenders a higher density of active sites compared to planar structure.

We applied *operando* Raman spectroscopy to confirm that CO was produced initially at Ag sites. The weak binding of CO to Ag favors desorption of CO and spillover to Cu sites[40, 61]. Remarkably, enhanced coverage of CH-containing intermediates on Cu was supported by new peaks (at 2713 and 2816 cm^{-1}) on our CuAg catalyst. These new findings strongly support our proposed CO spillover mechanism, which guides us towards the design of more efficient catalysts.

Based on the impressive performance of our cathode we realized a complete photosynthetic CO_2 reduction system using water as an electron and proton source, which is driven solely by solar light harvested by perovskite solar cells. The latter have recently emerged as an attractive contender for low-cost photovoltaics and provided the well-matched operating point for selective ethylene formation in our electrochemical device. This artificial photosynthetic system delivers a solar-to-ethylene free energy

conversion efficiency of 4.17% and a total solar-to-fuel conversion efficiency of 7.78% by accounting for all reduction products. The solar-to-ethylene conversion efficiency represents a benchmark in solar-driven CO_2 conversion systems. This study will not only enable fundamental understanding of how to optimize the interplay of activity and selectivity in CO_2 reduction, but also facilitate future progress on catalyst development. Our observations will assist the transformation from an observation-driven to a design-driven approach for photo-electrochemical CO_2 reduction.

ACKNOWLEDGEMENTS

This work was financially funded by Sino-Swiss Science and Technology Cooperation (SSSTC) 2016 under the project title "All perovskite tandems for solar to CO_2 fixation" from Swiss National Science Foundation (IZLCZ2–170294). J.G. is financially supported by an overseas exchange scholarship from China Scholarship Council (No. CSC201706370233). M.G. and H.Z. acknowledge the funding support from the European's Horizon 2020 research and innovation programme under grant agreement No. 764047. The authors gratefully thank Aurélien Bornet (NMR, ISIC, EPFL) for the technical support on ^{1}H NMR, Pierre Mettraux (SCI, EPFL) for the XPS characterization, Arnaud Magrez (IPHYS, EPFL) for assist in Raman spectroscopy and Zaiwei Wang (LSPM, EPFL) for the XRD measurement.

AUTHOR INFORMATION

Corresponding authors:

D.R.: dan.ren@epfl.ch,

M.G.: michael.graetzel@epfl.ch

Notes

The authors declare no competing financial interest.

ASSOCIATED CONETS

The Supporting Information is available free of charge on the ACS Publication Web site.

Additional characterizations of $Cu(OH)_2$, Cu_2O and Cu_2O-Ag; Characterizations of oxide-derived Cu and CuAg catalysts; Electrochemical reduction of carbon dioxide on Cu and CuAg; Faradaic efficiency and partial current density for products; CO_2 reduction on Ag nanocorals; CO_2 reduction on planar Cu_2O-Ag; Raman spectroscopic studies on Ag; SERS effect of Ag nanoparticles on Cu_2O; Calculation of CO spillover efficiency; CO_2 reduction on CuAu; Solar-driven CO_2 reduction

REFERENCES

1. Aresta, M.; Dibenedetto, A.; Angelini, A., Catalysis for the Valorization of Exhaust Carbon: from CO_2 to Chemicals, Materials, and Fuels. Technological Use of CO_2. *Chem. Rev.* **2013,** *114* (3), 1709-1742.
2. Greenblatt, J. B.; Miller, D. J.; Ager, J. W.; Houle, F. A.; Sharp, I. D., The Technical and Energetic Challenges of Separating (Photo)Electrochemical Carbon Dioxide Reduction Products. *Joule 2* (3), 381-420.
3. Hori, Y., Electrochemical CO_2 Reduction on Metal Electrodes. In *Modern Aspects of Electrochemistry*, Vayenas, C. G.; White, R. E.; Gamboa-Aldeco, M. E., Eds. Springer New York: 2008; Vol. 42, pp 89-189.
4. Kuhl, K. P.; Cave, E. R.; Abram, D. N.; Jaramillo, T. F., New Insights into the Electrochemical Reduction of Carbon Dioxide on Metallic Copper Surfaces. *Energy Environ. Sci.* **2012,** *5* (5), 7050-7059.
5. Hori, Y.; Kikuchi, K.; Suzuki, S., Production of CO and CH_4 in electrochemical reduction of CO_2 at metal electrodes in aqueous hydrogencarbonate solution. *Chem. Lett.* **1985,** (11), 1695-1698.
6. Hori, Y.; Murata, A.; Takahashi, R., Formation of Hydrocarbons in the Electrochemical Reduction of Carbon Dioxide at a Copper Electrode in Aqueous Solution. *J. Chem. Soc., Faraday Trans. 1* **1989,** *85* (8), 2309-2326.
7. Kas, R.; Kortlever, R.; Milbrat, A.; Koper, M. T. M.; Mul, G.; Baltrusaitis, J., Electrochemical CO_2 Reduction on Cu_2O-derived Copper Nanoparticles: Controlling the Catalytic Selectivity of Hydrocarbons. *Phys. Chem. Chem. Phys.* **2014,** *16* (16), 12194-12201.
8. Tang, W.; Peterson, A. A.; Varela, A. S.; Jovanov, Z. P.; Bech, L.; Durand, W. J.; Dahl, S.; Nørskov, J. K.; Chorkendorff, I., The Importance of Surface Morphology in Controlling the Selectivity of Polycrystalline Copper for CO_2 Electroreduction. *Phys. Chem. Chem. Phys.* **2012,** *14* (1), 76-81.
9. Huang, Y.; Handoko, A. D.; Hirunsit, P.; Yeo, B. S., Electrochemical Reduction

of CO_2 Using Copper Single-Crystal Surfaces: Effects of CO* Coverage on the Selective Formation of Ethylene. *ACS Catal.* **2017,** *7*, 1749-1756.
10. Ren, D.; Fong, J.; Yeo, B. S., The effects of currents and potentials on the selectivities of copper toward carbon dioxide electroreduction. *Nat. Commun.* **2018,** *9* (1), 925.
11. Ren, D.; Ang, B. S.-H.; Yeo, B. S., Tuning the Selectivity of Carbon Dioxide Electroreduction toward Ethanol on Oxide-Derived Cu_xZn Catalysts. *ACS Catal.* **2016,** *6* (12), 8239-8247.
12. Lee, S.; Park, G.; Lee, J., Importance of Ag–Cu Biphasic Boundaries for Selective Electrochemical Reduction of CO_2 to Ethanol. *ACS Catal.* **2017,** *7* (12), 8594-8604.
13. Gurudayal; Bullock, J.; Sranko, D. F.; Towle, C. M.; Lum, Y.; Hettick, M.; Scott, M. C.; Javey, A.; Ager, J., Efficient solar-driven electrochemical CO_2 reduction to hydrocarbons and oxygenates. *Energy Environ. Sci.* **2017,** *10* (10), 2222-2230.
14. Chang, Z.; Huo, S.; Zhang, W.; Fang, J.; Wang, H., The tunable and highly selective reduction products on Ag@Cu bimetallic catalysts toward CO_2 electrochemical reduction reaction. *J. Phys. Chem. C* **2017,** *121* (21), 11368-11379.
15. Clark, E. L.; Hahn, C.; Jaramillo, T. F.; Bell, A. T., Electrochemical CO_2 Reduction over Compressively Strained CuAg Surface Alloys with Enhanced Multi-Carbon Oxygenate Selectivity. *J. Am. Chem. Soc.* **2017,** *139* (44), 15848-15857.
16. Hoang, T. T. H.; Verma, S.; Ma, S.; Fister, T. T.; Timoshenko, J.; Frenkel, A. I.; Kenis, P. J. A.; Gewirth, A. A., Nanoporous Copper–Silver Alloys by Additive-Controlled Electrodeposition for the Selective Electroreduction of CO_2 to Ethylene and Ethanol. *J. Am. Chem. Soc.* **2018,** *140* (17), 5791-5797.
17. Morales-Guio, C. G.; Cave, E. R.; Nitopi, S. A.; Feaster, J. T.; Wang, L.; Kuhl, K. P.; Jackson, A.; Johnson, N. C.; Abram, D. N.; Hatsukade, T.; Hahn, C.; Jaramillo, T. F., Improved CO2 reduction activity towards C2+ alcohols on a tandem gold on copper electrocatalyst. *Nat. Catal.* **2018,** *1* (10), 764-771.
18. Giordano, F.; Abate, A.; Correa Baena, J. P.; Saliba, M.; Matsui, T.; Im, S. H.; Zakeeruddin, S. M.; Nazeeruddin, M. K.; Hagfeldt, A.; Graetzel, M., Enhanced electronic properties in mesoporous TiO2 via lithium doping for high-efficiency perovskite solar cells. *Nat. Commun.* **2016,** *7*, 10379.
19. Saliba, M.; Matsui, T.; Seo, J.-Y.; Domanski, K.; Correa-Baena, J.-P.; Nazeeruddin, M. K.; Zakeeruddin, S. M.; Tress, W.; Abate, A.; Hagfeldt, A., Cesium-containing triple cation perovskite solar cells: improved stability, reproducibility and high efficiency. *Energy Environ. Sci.* **2016,** *9* (6), 1989-1997.
20. McCrory, C. C. L.; Jung, S.; Ferrer, I. M.; Chatman, S. M.; Peters, J. C.; Jaramillo, T. F., Benchmarking Hydrogen Evolving Reaction and Oxygen Evolving Reaction Electrocatalysts for Solar Water Splitting Devices. *J. Am. Chem. Soc.* **2015,** *137* (13), 4347-4357.
21. Ren, D.; Loo, N. W. X.; Gong, L.; Yeo, B. S., Continuous Production of Ethylene from Carbon Dioxide and Water Using Intermittent Sunlight. *ACS Sustainable Chem. Eng.* **2017,** *5* (10), 9191-9199.

22. Schreier, M.; Héroguel, F.; Steier, L.; Ahmad, S.; Luterbacher, J. S.; Mayer, M. T.; Luo, J.; Grätzel, M., Solar conversion of CO_2 to CO using Earth-abundant electrocatalysts prepared by atomic layer modification of CuO. *Nat. Energy* **2017,** *2*, 17087.
23. Bakthavatsalam, R.; Kundu, J., A galvanic replacement-based Cu_2O self-templating strategy for the synthesis and application of Cu_2O–Ag heterostructures and monometallic (Ag) and bimetallic (Au–Ag) hollow mesocages. *CrystEngComm* **2017,** *19* (12), 1669-1679.
24. Chook, S. W.; Chia, C. H.; Zakaria, S.; Ayob, M. K.; Chee, K. L.; Huang, N. M.; Neoh, H. M.; Lim, H. N.; Jamal, R.; Rahman, R., Antibacterial performance of Ag nanoparticles and AgGO nanocomposites prepared via rapid microwave-assisted synthesis method. *Nanoscale Res. Lett.* **2012,** *7* (1), 541.
25. Deo, M.; Mujawar, S.; Game, O.; Yengantiwar, A.; Banpurkar, A.; Kulkarni, S.; Jog, J.; Ogale, S., Strong photo-response in a flip-chip nanowire p-Cu_2O/n-ZnO junction. *Nanoscale* **2011,** *3* (11), 4706-4712.
26. Ren, D.; Deng, Y.; Handoko, A. D.; Chen, C. S.; Malkhandi, S.; Yeo, B. S., Selective Electrochemical Reduction of Carbon Dioxide to Ethylene and Ethanol on Copper(I) Oxide Catalysts. *ACS Catal.* **2015,** *5* (5), 2814-2821.
27. Pander Iii, J. E.; Ren, D.; Yeo, B. S., Practices for the collection and reporting of electrocatalytic performance and mechanistic information for the CO2 reduction reaction. *Catal. Sci. Technol.* **2017,** *7* (24), 5820-5832.
28. Gupta, N.; Gattrell, M.; MacDougall, B., Calculation for the cathode surface concentrations in the electrochemical reduction of CO_2 in $KHCO_3$ solutions. *J. Appl. Electrochem.* **2005,** *36* (2), 161-172.
29. Hall, A. S.; Yoon, Y.; Wuttig, A.; Surendranath, Y., Mesostructure-induced selectivity in CO_2 reduction catalysis. *J. Am. Chem. Soc.* **2015,** *137* (47), 14834-14837.
30. Clark, E. L.; Resasco, J.; Landers, A.; Lin, J.; Chung, L.-T.; Walton, A.; Hahn, C.; Jaramillo, T. F.; Bell, A. T., Standards and Protocols for Data Acquisition and Reporting for Studies of the Electrochemical Reduction of Carbon Dioxide. *ACS Catal.* **2018,** *8* (7), 6560-6570.
31. Calle-Vallejo, F.; Koper, M. T. M., Theoretical Considerations on the Electroreduction of CO to C_2 Species on Cu(100) Electrodes. *Angew. Chem. Int. Ed.* **2013,** *52* (28), 7282-7285.
32. Montoya, J. H.; Peterson, A. A.; Nørskov, J. K., Insights into C-C Coupling in CO_2 Electroreduction on Copper Electrodes. *ChemCatChem* **2013,** *5* (3), 737-742.
33. Schouten, K. J. P.; Qin, Z.; Pérez Gallent, E.; Koper, M. T., Two pathways for the formation of ethylene in CO reduction on single-crystal copper electrodes. *J. Am. Chem. Soc.* **2012,** *134* (24), 9864-9867.
34. Sen, S.; Liu, D.; Palmore, G. T. R., Electrochemical Reduction of CO2 at Copper Nanofoams. *ACS Catal.* **2014,** *4* (9), 3091-3095.
35. Handoko, A. D.; Chan, K. W.; Yeo, B. S., –CH_3 Mediated Pathway for the Electroreduction of CO_2 to Ethane and Ethanol on Thick Oxide-Derived Copper

Catalysts at Low Overpotentials. *ACS Energy Lett.* **2017,** *2* (9), 2103-2109.
36. Kim, D.; Lee, S.; Ocon, J. D.; Jeong, B.; Lee, J. K.; Lee, J., Insights into an autonomously formed oxygen-evacuated Cu_2O electrode for the selective production of C_2H_4 from CO_2. *Phys. Chem. Chem. Phys.* **2015,** *17* (17), 824-830.
37. Ren, D.; Gao, J.; Pan, L.; Wang, Z.; Luo, J.; Zakeeruddin, S. M.; Hagfeldt, A.; Grätzel, M., Atomic Layer Deposition of ZnO on CuO Enables Selective and Efficient Electroreduction of Carbon Dioxide to Liquid Fuels. *Angew. Chem. Int. Ed.* **2019**.
38. Oda, I.; Ogasawara, H.; Ito, M., Carbon monoxide adsorption on copper and silver electrodes during carbon dioxide electroreduction studied by infrared reflection absorption spectroscopy and surface-enhanced Raman spectroscopy. *Langmuir* **1996,** *12* (4), 1094-1097.
39. Wood, T. H.; Klein, M. V., Raman scattering from carbon monoxide adsorbed on evaporated silver films. *J. Vac. Sci. Technol* **1979,** *16* (2), 459-461.
40. Kuhl, K. P.; Hatsukade, T.; Cave, E. R.; Abram, D. N.; Kibsgaard, J.; Jaramillo, T. F., Electrocatalytic Conversion of Carbon Dioxide to Methane and Methanol on Transition Metal Surfaces. *J. Am. Chem. Soc.* **2014,** *136* (40), 14107-14113.
41. Li, Y. C.; Wang, Z.; Yuan, T.; Nam, D.-H.; Luo, M.; Wicks, J.; Chen, B.; Li, J.; Li, F.; de Arquer, F. P. G.; Wang, Y.; Dinh, C.-T.; Voznyy, O.; Sinton, D.; Sargent, E. H., Binding Site Diversity Promotes CO2 Electroreduction to Ethanol. *J. Am. Chem. Soc.* **2019,** *141* (21), 8584-8591.
42. Liu, X.; Xiao, J.; Peng, H.; Hong, X.; Chan, K.; Nørskov, J. K., Understanding trends in electrochemical carbon dioxide reduction rates. *Nat. Commun.* **2017,** *8*, 15438.
43. Ichinohe, Y.; Wadayama, T.; Hatta, A., Electrochemical reduction of CO2 on silver as probed by surface-enhanced Raman scattering. *J. Raman Spectrosc.* **1995,** *26* (5), 335-340.
44. Schouten, K. J. P.; Qin, Z.; Pérez Gallent, E.; Koper, M. T. M., Two Pathways for the Formation of Ethylene in CO Reduction on Single-Crystal Copper Electrodes. *J. Am. Chem. Soc.* **2012,** *134* (24), 9864-9867.
45. Pander III, J. E.; Ren, D.; Huang, Y.; Loo, N. W. X.; Hong, S. H. L.; Yeo, B. S., Understanding the Heterogeneous Electrocatalytic Reduction of Carbon Dioxide on Oxide-Derived Catalysts. *ChemElectroChem* **2018,** *5* (2), 219-237.
46. Pérez-Gallent, E.; Figueiredo, M. C.; Calle-Vallejo, F.; Koper, M. T. M., Spectroscopic Observation of a Hydrogenated CO Dimer Intermediate During CO Reduction on Cu(100) Electrodes. *Angew. Chem. Int. Ed.* **2017,** *56* (13), 3621-3624.
47. Deng, Y.; Ting, L. R. L.; Neo, P. H. L.; Zhang, Y.-J.; Peterson, A. A.; Yeo, B. S., Operando Raman Spectroscopy of Amorphous Molybdenum Sulfide (MoS_x) during the Electrochemical Hydrogen Evolution Reaction: Identification of Sulfur Atoms as Catalytically Active Sites for H^+ Reduction. *ACS Catal.* **2016**, 7790-7798.
48. Kortlever, R.; Shen, J.; Schouten, K. J. P.; Calle-Vallejo, F.; Koper, M. T. M., Catalysts and Reaction Pathways for the Electrochemical Reduction of Carbon Dioxide. *J. Phy. Chem. Lett.* **2015,** *6*, 4073-4082.
49. Hsieh, Y.-C.; Senanayake, S. D.; Zhang, Y.; Xu, W.; Polyansky, D. E., Effect of

chloride anions on the synthesis and enhanced catalytic activity of silver nanocoral electrodes for CO_2 electroreduction. *ACS Catal.* **2015,** *5* (9), 5349-5356.
50. Verdaguer-Casadevall, A.; Li, C. W.; Johansson, T. P.; Scott, S. B.; McKeown, J. T.; Kumar, M.; Stephens, I. E. L.; Kanan, M. W.; Chorkendorff, I., Probing the Active Surface Sites for CO Reduction on Oxide-Derived Copper Electrocatalysts. *J. Am. Chem. Soc.* **2015,** *137* (31), 9808-9811.
51. Joshi, U.; Malkhandi, S.; Yeo, B. S., Investigating synergistic interactions of group 4, 5 and 6 metals with gold nanoparticles for the catalysis of the electrochemical hydrogen evolution reaction. *Phys. Chem. Chem. Phys.* **2017,** *19* (31), 20861-20866.
52. Joshi, U.; Lee, J.; Giordano, C.; Malkhandi, S.; Yeo, B. S., Enhanced catalysis of the electrochemical hydrogen evolution reaction using composites of molybdenum-based compounds, gold nanoparticles and carbon. *Phys. Chem. Chem. Phys.* **2016,** *18* (31), 21548-21553.
53. Gao, J.; Ren, D.; Guo, X.; Zakeeruddin, S. M.; Grätzel, M., Sequential Catalysis Enables Enhanced C-C Coupling towards Multicarbon Alkenes and Alcohols in Carbon Dioxide Reduction: A Study on CuAu Electrocatalysts. *Faraday Discuss.* **2019,** *215*, 282-296.
54. Schreier, M.; Curvat, L.; Giordano, F.; Steier, L.; Abate, A.; Zakeeruddin, S. M.; Luo, J.; Mayer, M. T.; Grätzel, M., Efficient Photosynthesis of Carbon Monoxide from CO_2 Using Perovskite Photovoltaics. *Nat. Commun.* **2015,** *6*, 7326.
55. Asadi, M.; Kim, K.; Liu, C.; Addepalli, A. V.; Abbasi, P.; Yasaei, P.; Phillips, P.; Behranginia, A.; Cerrato, J. M.; Haasch, R., Nanostructured Transition Metal Dichalcogenide Electrocatalysts for CO_2 Reduction in Ionic Liquid. *Science* **2016,** *353* (6298), 467-470.
56. Zhou, X.; Liu, R.; Sun, K.; Chen, Y.; Verlage, E.; Francis, S. A.; Lewis, N. S.; Xiang, C., Solar-Driven Reduction of 1 atm of CO_2 to Formate at 10% Energy-Conversion Efficiency by Use of a TiO_2-Protected III–V Tandem Photoanode in Conjunction with a Bipolar Membrane and a Pd/C Cathode. *ACS Energy Lett.* **2016,** *1* (4), 764-770.
57. Arai, T.; Sato, S.; Morikawa, T., A Monolithic Device for CO_2 Photoreduction to Generate Liquid Organic Substances in a Single-Compartment Reactor. *Energy Environ. Sci.* **2015,** *8* (7), 1998-2002.
58. Kniel, L.; Winter, O.; Stork, K., *Ethylene, keystone to the petrochemical industry*. M. Dekker: New York, 1980.
59. Huan, T. N.; Dalla Corte, D. A.; Lamaison, S.; Karapinar, D.; Lutz, L.; Menguy, N.; Foldyna, M.; Turren-Cruz, S. H.; Hagfeldt, A.; Bella, F.; Fontecave, M.; Mougel, V., Low-cost high-efficiency system for solar-driven conversion of CO_2 to hydrocarbons. *Proc. Natl. Acad. Sci. U. S. A.* **2019,** *116* (20), 9735-9740.
60. Singh, M. R.; Clark, E. L.; Bell, A. T., Thermodynamic and Achievable Efficiencies for Solar-Driven Electrochemical Reduction of Carbon Dioxide to Transportation Fuels. *Proc. Natl. Acad. Sci.* **2015,** *112* (45), E6111-E6118.
61. Gurudayal, G.; Perone, D.; Malani, S.; Lum, Y.; Haussener, S.; Ager, J. W.,

Sequential Cascade Electrocatalytic Conversion of Carbon Dioxide to C-C Coupled Products. *ACS Appl. Energy Mater.* **2019,** *2* (6), 4551-4559.

TOC Figure

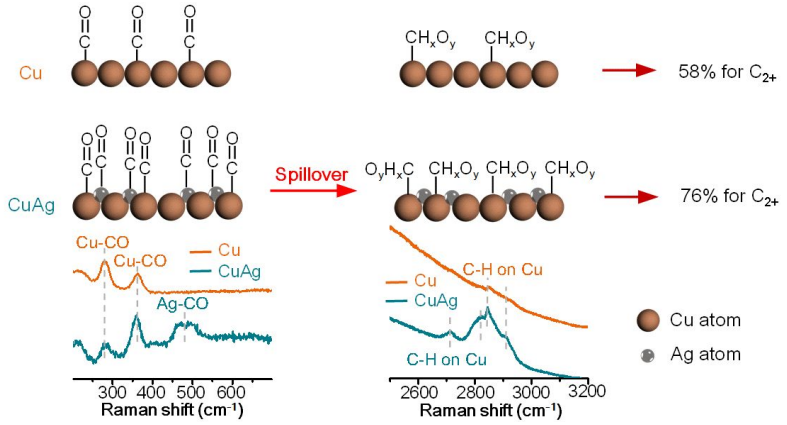
Cu
CuAg
Spillover
58% for C_{2+}
76% for C_{2+}
Cu-CO
Cu-CO
Ag-CO
Cu
CuAg
300 400 500 600
Raman shift (cm⁻¹)
C-H on Cu
C-H on Cu
Cu
CuAg
2600 2800 3000 3200
Raman shift (cm⁻¹)
Cu atom
Ag atom